Axial Position Estimation of Conical Shaped Motors for Aerospace Traction Applications

S. Roggia, F. Cupertino, *Senior Member, IEEE,* C. Gerada, *Member, IEEE,* M. Galea, *Member, IEEE*

***Abstract* – This paper is concerned with the use of conical induction machines. Such machines are extremely valuable when apart from the rotational torque output, an axial translation of the rotor is also required. The inherent attraction between the stator and rotor of any machine, combined with the geometry of a conical machine will provide the required axial movement. However, when applied to aerospace applications, where reliability is very important, then full monitoring of the axial position is required. In this paper, an innovative approach aimed at monitoring and controlling the axial translation of a conical induction machine is proposed and investigated. In order to increase the system reliability and also decrease component count, as demanded by the application, the methodology is a sensor-less technique, based on an innovative variant of the high-frequency injection approach. In this paper, the technique has been fully investigated and experimentally validated on a purposely-built, instrumented test-rig.**

***Index Terms*--conical motor; sliding rotor; high voltage signal injection; in-wheel actuator.**

I. INTRODUCTION

In the context of the more electric aircraft (MEA), a particular traction application [1-12] for aerospace requires an electrical motor to be integrated into the landing gear (LG) of an aircraft.

The proposed solution for the application at hand is a direct drive (DD), permanently engaged wheel actuator (WA). The WA itself consists in a high torque density, permanent magnet (PM) motor [13-15].This technology has been chosen in order to meet peak torque requirements within the maximum accessible volume inside the LG. In the DD configuration, the motor is directly connected to the wheel without any reduction gearbox. This means that the machine will always spin at the same speed of the wheel. However, during high wheel speed phases, such as landing and take-off, the wheel of the aircraft can reach high levels of velocity. As the PM machine is designed for the "normal" taxiing speeds, excessively high voltages can be expected at high speeds. Therefore a new system arrangement is desirable.

Potential solutions are an active clutch, as presented in [9, 10, 16] or an integrated clutch. While these two schemes would work perfectly, however, they would come at the cost of an increase in component count and weight. Other perceived drawbacks are the risk of mechanical jamming, associated with the presence of mechanical parts, and the reduction of the space allocated for the motor that in turn implies a decrease of motor's performances.

As suggested in [17], the implementation of a conical actuator [18] enables to have a physical, "active" disconnection mechanism between the motor and the wheel without having to rely on extra components.

A conical motor is an electrical machine in which the internal surface of the stator and the rotor have a tapered shape. This means that a conical air gap exists between the stator and the rotor, as shown in Fig. 1.

The magnetic force, resulting from the interaction between the rotating and steady part of the motor, is perpendicular to the rotor surface and contains an axial contribution responsible for the horizontal movement of the rotor [19]. The axial component of the force, in fact, causes a translational movement of the rotor that occurs conjointly with the rotational one.

When the rotor is moving inside-out of the stator, the motor will perform an active engagement or disengagement of the wheel. Thus, the detachment of the rotor during landing and take-off will prevent the motor from any damage (mechanical and/or electrical) whilst the presence of any additional mechanical coupling is still avoided (i.e. gearbox).

In order to prove the concept of the engagement/disengagement with conical machines, an "off-the-shelf" conical induction motor (IM) [20] has been utilized. The commercial machine in its actual application is employed as a braking motor. The braking system is composed of a disk and a spring, as clearly observed in Fig. 1.

For such a conical IM, the axial force mentioned above will pull the rotor inside the stator whereas the spring, embedded in the machine, pushes the rotor back.

The axial force produced by the motor is fundamental for the rotor horizontal displacement, however, the evaluation of this force is not related to the monitoring aspects of the axial movement. Thus, this paper is exclusively concerned with an axial position estimation procedure for the conical IM based on the motor features.

The axial monitoring system represents an additional measure of safety that should be implemented within the whole system in order to prove that the motor is correctly engaged to the wheel. Traditionally, linear positioning has always been achieved by the use of sensors such as for example linear encoders. However, for the aerospace application at hand, this is not ideal as again this would be increasing component count.

Apart from space limitations, the inherent fragility and low robustness of sensors can be a significant limiting factor, also due to the high level of vibration and temperature inside the landing gear [21].

A solution to this particular problem is to adapt a reliable and accurate sensorless technique for the application and requirements at hand, i.e. a transducer-less position monitoring methodology for the axial position of the conical IM.

Over the last decade, sensor-less techniques for electric machine control have become a common and robust [22], way to achieve high levels of reliability, especially where costs need to be reduced and the space allocated to the drive represents a compelling factor [23]. The main sensor-less methods can be categorized as fundamental wave based (i.e. observer EMF Models, Flux Modulation, etc.) and anisotropies exploitation methods (i.e. *dq* inductances, slot asymmetries, etc.)[20][24-27].

While all the above have been demonstrated and proven, however in this paper, the aim is to propose and investigate a sensorless technique for axial position monitoring of a conical IM. To the authors' knowledge, this is not found in literature mainly because there are no similar applications and no sensorless position estimation (axial or rotational) have been ever performed on a conical shaped machine

The aim of this paper is thus to propose and investigate a sensorless technique for monitoring and controlling the rotor's axial position. In the next sections, the proposed technique is introduced and experimental results are exposed in order to illustrate how the investigated phenomena match the expected theoretical behavior of the motor.

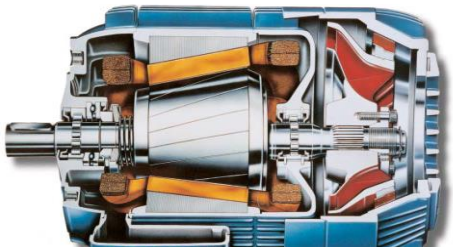

Fig. 1 - Conical Induction Motor Cross Section [20]

II. Axial Position Estimation Procedure

The axial position of the rotor can be estimated by using the motor itself as a sensor (*self-sensing* technique). In this research work, in fact, a traditional sensorless method, based on the exploitation of saliency due to the saturation of the main path [28-30] has been adopted. The axial position of the rotor inside the stator is evaluated by detecting changes in motor features with axial rotor position as described in the next section.

The proposed strategy takes advantage of the variation in magnetic features of the actuator when the rotor is moving axially in and out of the stator. As the conical motor is moving between full extension and full retraction, it is clear that the air-gap's length is also changing. This means that as the rotor is moving, the machine's main magnetic circuit is also changing, and the machine flux and its paths will be dependent on each instantaneous axial position of the rotor. This also indicates that saturation levels in the machine will be in constant transients, which allows for very valuable information to be gained and exploited from the effects of saturation.

The tendency of the motor to be saturated can be expressed by the inductance parameters. The *magnetic saliency*, defined as the variation in *stator inductance* measured at motor terminals, quantifies the rate of change in the motor parameters due to saturation. Saliency can be utilized to evaluate the axial position of the rotor.

A. The basic Theory and Concept

Fig. 2, gives the generic relationship between the angular coefficient of the flux-current curve and the stator inductance. During axial movements of the rotor, the *flux-current characteristic* of the motor translates from the right to the left in the ϕ-$\mathbf{i}_S$ plane, also highlighting that the stator inductance varies accordingly. However, if the main magnetic circuit of the machine is already heavily saturated, then the machine's total inductance is not so dependent on the axial movement and position. In the same figure, when any particular working point close to saturation is considered, the angular coefficients of the two curves become very similar whereas the tangents to the flux-current characteristics, assume appreciable different inclinations.

Thus, if these saturation effects are tracked and made to relate to an appropriate parameter, that parameter can be said to represent the axial position of the rotor. This will then allow for a sensor-less, position monitoring scheme to be implemented.

As stated in the literature, *High Frequency (HF) Injection Technique* represents an efficient method to analyze the effect of *saturation* in the machine and track the *magnetic saliency*, especially in applications at zero or low speed [21, 29]. This methodology takes advantage of the interaction between the *carrier signal* excitation and the stator transient inductance to estimate machine parameters [28]. In fact, saturation effects induced in the machine are capable to spatially modulate the quantity $\sigma\mathbf{L}_S$. The response of the motor to the *carrier signal* contains information about saliency. Namely, when a *high-frequency voltage* signal is injected (*carrier voltage signal*) the current response can be demodulated and examined in order to gain this information. The *carrier current response* contains one *positive* and one *negative sequence* [24]. These two contributions can be analyzed separately in order to get the necessary information. In the present work, the *negative sequence current* will be monitored in order to assess the axial position of the motor.

The axial movement is realized by acting on the *magnetizing current*, $\boldsymbol{i}_s^d$. The magnetizing current, in fact, produces the necessary magnetic force, responsible for the attraction between the rotor and the stator. The amplitude of the *negative sequence current* is strictly dependent on the magnetizing

current. These two parameters will be influential in determining the axial rotor position.

As a result, monitoring the negative counterpart of the high-frequency current, for each level of the magnetizing current, and relating this quantity to the axial position of the rotor is the core aspect of the exposed method.

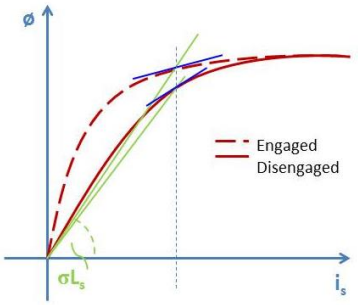

Fig. 2 - Stator Transient Inductance Representation in Flux-Current Reference Frame

B. *High-Frequency Signal Injection*

In the proposed scheme, the *conical IM* has been modeled in a similar manner as for rotational IMs, i.e. using space vectors. The voltage equations are expressed either in the time-dependent stationary reference frame $\alpha\beta$ as given in (1) and/or in the time-independent synchronous reference frame dq as described by (2), where subscripts S and R refer to stator and rotor quantities respectively, L_M is the magnetizing inductance, $\sigma\mathbf{L}_S$ is the *stator transient inductance*, ω_φ is the angular speed of rotor flux space vector (λ_R) and σ is the *leakage factor* as described by (3).

$$\mathbf{u}_s^{\alpha\beta} = R_s\mathbf{i}_s^{\alpha\beta} + \sigma\mathbf{L}_s\frac{d\mathbf{i}_s^{\alpha\beta}}{dt} + \frac{L_M}{L_R}\frac{d\boldsymbol{\lambda}_R}{dt} \tag{1}$$

$$\mathbf{u}_s^{dq} = R_s\mathbf{i}_s^{dq} + \sigma\mathbf{L}_s\frac{d\mathbf{i}_s^{dq}}{dt} + \frac{L_M}{L_R}\frac{d\boldsymbol{\lambda}_R}{dt} + j\omega_\varphi\sigma\mathbf{L}_s^{dq} + j\omega_R\frac{L_M}{L_R}\boldsymbol{\lambda}_R \tag{2}$$

$$\sigma = \frac{1 - L_M{}^2}{L_R L_s} \tag{3}$$

When the high-frequency carrier signal is superimposed on the fundamental excitation, the behavior of the motor at high frequencies can be modeled as in (4). If the injection frequency ω_{Inj} is sufficiently higher than the fundamental, then the voltage drop on the resistance can be neglected and the model can be approximated by using the stator transient inductance, as the carrier signal excitation is faster than the stator transient constant time [31-35]:

$$\mathbf{u}_{shf}^{\alpha\beta} \cong j\omega_{Inj}\sigma\mathbf{L}_s^{\alpha\beta}\mathbf{i}_{shf}^{\alpha\beta}\,. \tag{4}$$

The rotating high-frequency voltage $\boldsymbol{u}_{shf}^{\alpha\beta}$ is generated by injecting, in the stationary frame $\alpha\beta$, two continuous signals with same amplitude (U_{Inj}) and frequency (ω_{Inj}). The injected signal, describing a circumference in the stationary reference frame, with radius equal to U_{Inj} and centre in the origin of the reference frame, is implemented in the following form:

$$\mathbf{u}_{shf}^{\alpha\beta} = \begin{bmatrix} u_{shf}^{\alpha} \\ u_{shf}^{\beta} \end{bmatrix} = U_{Inj}\begin{bmatrix} \cos\omega_{Inj}t \\ \sin\omega_{Inj}t \end{bmatrix} = U_{Inj}e^{j\omega_{Inj}t}\,. \tag{5}$$

The *stator transient inductance*, containing saturation-induced saliency, in the saliency synchronous reference frame can be represented as follow:

$$\sigma\mathbf{L}_s^{dq} = \begin{bmatrix} \sigma L_s^d & 0 \\ 0 & \sigma L_s^q \end{bmatrix}. \tag{6}$$

When transformed to the stationary (stator) reference frame, the stator transient inductance can be expressed as the sum of two quantities, as shown in (7), where ϑ_e is the *angle of rotating saliency* and where the *average stator inductance* $\sum\sigma\mathbf{L}_S$ *and the differential stator transient inductance* $\Delta\sigma\mathbf{L}_S$ are given in (8) and (9) respectively.

$$\sigma\mathbf{L}_S^{\alpha\beta} = \begin{bmatrix} \sum\sigma L_S + \Delta\sigma L_S\cos(2\vartheta_e) & -\Delta\sigma L_S\sin(2\vartheta_e) \\ -\Delta\sigma L_S\sin(2\vartheta_e) & \sum\sigma L_S - \Delta\sigma L_S\sin(2\vartheta_e) \end{bmatrix} \tag{7}$$

$$\sum\sigma L_s = \frac{\sigma L_s^q + \sigma L_s^d}{2} \tag{8}$$

$$\Delta\sigma L_s = \frac{\sigma L_s^q - \sigma L_s^d}{2} \tag{9}$$

Due to the interaction between the magnetic saliency and the voltage carrier signal, a *carrier current signal*, $\boldsymbol{i}_{shf}$, with same the frequency of the injected voltage (ω_{Inj}), is induced in the stator. The high frequency currents signal consists of *positive and negative sequence* components and they can be summarized as in (10).

$$\mathbf{i}_{shf} = i_{sp}e^{j\omega_{inj}t} + \sum_m\sum_k i_{sn_{mk}}e^{-j(\omega_{inj}t + h_{mk}\vartheta_m)} \tag{10}$$

The negative sequence current arises from different topologies of saliency [36-38]. Saliency due to rotor eccentricity can be neglected since exploitable in commercial machine [37]. When the specific case of *saturation saliency* in correspondence of m_1=1 and $\vartheta_1=\omega_e t$ is considered [30], the total *high-frequency* current can be expressed in the stationary reference frame $\alpha\beta$ as shown in (11) and where I_p and I_n are the amplitudes of the positive and negative sequence respectively, of the carrier current signal, as described in (12).

$$\begin{aligned}\mathbf{i}_{shf}^{\alpha\beta} &= \begin{bmatrix} i_{shf}^{\alpha} \\ i_{shf}^{\beta} \end{bmatrix} = \begin{bmatrix} I_p\cos\omega_{Inj}t + I_n\cos(2\vartheta_e - \omega_{Inj}t) \\ I_p\sin\omega_{Inj}t + I_n\sin(2\vartheta_e - \omega_{Inj}t) \end{bmatrix} = \\ &= I_p e^{j\omega_{Inj}t} + I_n e^{j(2\vartheta_e - \omega_{Inj}t)} = \mathbf{i}_p^{\alpha\beta} + \mathbf{i}_n^{\alpha\beta}\end{aligned} \tag{11}$$

$$I_p = \frac{U_{Inj}}{\omega_{Inj}}\frac{\sum\sigma L_s}{\sum\sigma L_s^2 - \Delta\sigma L_s^2}; \qquad I_n = \frac{U_{Inj}}{\omega_{Inj}}\frac{\Delta\sigma L_s}{\sum\sigma L_s^2 - \Delta\sigma L_s^2} \tag{12}$$

The positive sequence is proportional to the *average stator transient inductance* $\sum\sigma\mathbf{L}_S$ whereas the negative sequence of the carrier signal current is proportional to *the differential stator inductance* $\Delta\sigma\mathbf{L}_S$.

When the motor moves from a completely disengaged

position to fully engaged position, the magnetic saliency becomes more significant. The saturation effects due to the high-frequency injection are at a maximum when the stator and rotor are fully aligned. When moving from one position to another, both the *average* $\sum\sigma\mathbf{L_s}$ and *the differential*, $\Delta\sigma\mathbf{L}_s$, *stator inductances* increase. However, $\Delta\sigma\mathbf{L}$ presents a considerably larger increment than the $\sum\sigma\mathbf{L_s}$. Due to its direct proportionality to $\Delta\sigma\mathbf{L}_s$ quantity, the *amplitude of the negative sequence signal* (I_n) will represent the signal of interest for the axial position tracking.

It is important to note that the amplitude of both sequences is strictly dependent on the choice of the injection frequency. If the chosen injected frequency is too high, the amplitude of the *high-frequency* currents reduces; and thus, difficulties can be faced during the tracking procedure. On the other hand, if the injection frequency is very close to the speed and current control loop bandwidths, the performances of the control scheme will be affected. Practical understanding of these effects is given in the next section.

C. Filtering

From all the above it is clear that whilst the high-frequency *negative-sequence* component of the current will be used for the axial position computation, the fundamental frequency counterpart will operate as the feedback signal for the current control loop.

Thus, the whole current signal needs to be processed and demodulated in order to isolate two different frequency levels of the current. This operation is implemented by means of two different filtering actions.

The feedback current of the current control loop component is obtained excluding the injection frequency component of the current with a Notch Filter.

The demodulation of the negative sequence carrier current can be achieved by shifting the negative-sequence to dc through the use of a new reference frame and attenuating the fundamental frequency current component by means of a *Low Pass Filter (LPF)*. Current carrier signal in the negative sequence synchronous frame is calculated as following:

$$\mathbf{i}_s^n = \mathbf{i}_{shf}\, e^{j(\omega_{Inj}t - 2\vartheta_e)}. \tag{13}$$

The operation has been implemented in a Simulink model that reproduces the block of Fig. 3 designated as "Filtering and Demodulation" block.

In order to associate the axial position to a certain amplitude of the *negative sequence* of the current, a *Look Up Table (LUT)* is essential. The *axial position* (x) is determined by *negative sequence signal* (I_n). However, since the amplitude of I_n is strictly related to level of *magnetizing current* ($\boldsymbol{i}_s^d$), a specific axial position will be determined by the level of $\boldsymbol{i}_s^d$ and I_n current in a 3D map.

$$x = f(\mathbf{i}_s^d, I_n)$$

The *LUT* has three dimensions. Values of the negative sequence current amplitude have been estimated and recorded by using the mean value of the *high-frequency* current in negative sequence reference frame:

$$I_n = mean(|\mathbf{i}_s^n|). \tag{14}$$

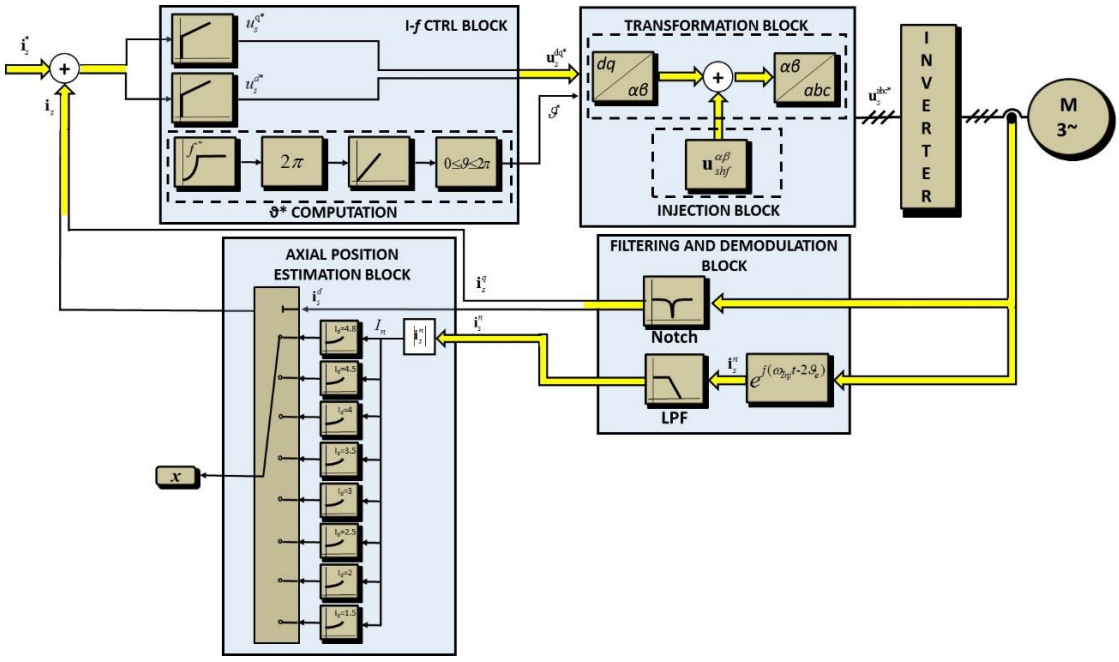

Fig. 3 - Axial Estimation and Control Diagram

This reiterative procedure has been executed for each position at each level of magnetizing current in order to obtain a LUT similar to the one reported in Fig. 11 of the experimental section.

D. Implementation

The *3D LUT* built through the mapping procedure can be also obtained from the interpolation between parallel planes (x, I_n) in which the magnetizing current ($\boldsymbol{i}_s^d$) represents a constant value and the axial position is obtained as function of the negative sequence signal amplitude (I_n).

$$x = f(\mathbf{i}_s^d, I_n) \rightarrow x = f(I_n)\big|_{\mathbf{i}_s^d}$$

Each (x, I_n) plane can be reported in a *2D LUT*. The level of magnetizing current, in this case, will be used for choosing between different *2D LUTs*. Each *2D LUT* will contain curves that relate the axial position to the amplitude of the negative sequence of the current.

This strategy has been opted in order to make the entire axial estimation procedure smoother and with the aim of having more accurate results. The scheme has been implemented in the "Axial Position Estimation Block" of Fig. 3.

The 2D *LUTs* of Fig. 4 receive as input the output of the *LPF* of the filtering block of Fig. 3. The system will choose the most appropriate 2D *LUT* standing on the measured values of the feedback magnetizing current signal (output of the Notch filter) and consequently return the rotor axial position.

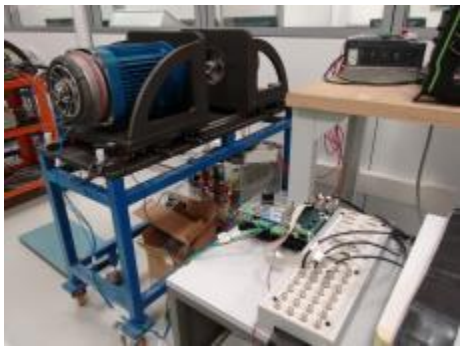

Fig. 4 - Experimental Test-rig

III. Experimental Set-Up

The axial position estimation method has been tested on an "off-the-shelf" conical motor with a rated speed of 500 rpm, 14 Nm torque at 50 Hz frequency, 4.8A current for wye connected 400 V voltage supply. As a default configuration, the rotor is always disengaged from the stator (similar to a normally off condition) due to the presence of the spring. In correspondence of the rated current, the motor will develop an axial force able to overcome the spring thrust. The spring described in Fig. 1will be compressed and the rotor will align to the stator. The brake spring force is 182*N* and clearance from completely disengaged to completely engaged position is 4 mm.

The real-time control of the motor has been realized through a dSPACE® Digital Signal Processing (DSP) board connected to a PC. The monitoring is performed using dSPACE software graphical user interface (GUI). The control algorithm has been built in *Matlab/Simulink*® environment and then converted and loaded onto the dSPACE DSP. Three A/D converters were used to transduce the feedback current signal and the DC link voltage measurements. A converter of 750 W rated power has been employed to feed the motor, equipped with three phase IGBT inverter. IGBTs features are: 4 Arms rated current, 400 DC V rated voltage and 24 kHz switching frequency. A picture of the complete experimental setup is given in Fig. 4.

In order to build and implement the axial estimation procedure, different topologies of tests have been carried out. Each of the experiments has the aim of separately developing the steps mentioned in Section II.

A. High-Frequency Signal Selection

As mentioned above, frequency injection techniques depend heavily on the right choice of the signal to be injected. In order to do this, several tests were performed on the machine on a range of frequencies from 100 to 1000 Hz and for different amplitudes of the injected signal. The tests consist in an exercise to estimate the rate of change of the negative-sequence of the carrier current signal when a magnetizing current sequence of steps is applied. The magnetizing current sequence increases until the engagement is reached. Starting from this point, a symmetrically decreasing sequence is performed for returning to disengaged position (Fig. 5). The rotor stays at the initial 0mm position until the rated current is reached, at which point the rotor moves to the 4mm extended position. The fully engaged position is maintained until the force of the motor prevails again: this happens when the magnetizing current reaches values lower than 2A.

Using the same sequence, with different injection signals, levels of negative sequence current have been recorded by using (14) and processed by comparing the level of negative-sequence signals obtained with different injection frequencies. From these procedures, it was found that the better-performing operation points were for signals in the region of 500 Hz voltage injection. An example has been reported in Fig. 6, where the trends of I_n amplitude with a 500Hz and 1000Hz injected signals are displayed. The magnitude of I_n has been reported for each level of magnetizing current $\boldsymbol{i}_s^d$. The left-hand side graph of Fig. 6 represents the level of negative-sequence current before the engagement happens and the axial position is equal to 0mm; the values correspond to the first part of the magnetizing current sequence of Fig. 5. On the right-hand side of Fig. 6, experimental results are reported for the descending part of the magnetizing current sequence of Fig. 5 when the rotor is in the extended position (4mm). The negative-sequence current amplitude with 500Hz injected voltage is two times greater than the one produced by using 1000 Hz injected signal; this is particularly noticeable when the rotor is engaged.

In the same way, the magnitude of the saturation reflected signal increases for a signal injection at lower frequencies. This effect makes easier the tracking procedure the negative sequence signal amplitude. However, if the frequency is close to the current control loop frequency, some issues can be experienced in the regulation of the current.

Since the amplitude of the negative current results easier to monitor when a 500Hz signal is adopted, all the experiments have been conducted by injecting a 500Hz-120V voltage. The amplitude of the carrier signal has been selected in accordance with the converter ratings.

B. Filtering

The filtering and demodulation actions have been implemented in the *Simulink* scheme that will generate the code to be downloaded on the DSP board. The demodulation operation of (13) occurs in the "Filtering and Demodulation" block of the scheme reported in Fig. 3. The output signal of the block represents the current in a reference frame synchronous with negative sequence signal. This signal has been filtered by means of a *Low Pass Filter* (LPF) with 70dB attenuation in correspondence of 500Hz (see magnitude response reported in Fig. 7). Different filters have been designed by means of traditional methods (i.e. Butterworth) [39] and compared in order to reach the lowest level of noise in the output signal with the smallest time delay.

The Notch Filter, utilized for obtaining the current feedback deprived of the high-frequency signal, has been centered in correspondence of 500 Hz as being the chosen injection frequency (Fig. 8). The output of this filter represents the input of the feedback signal of the current control loop.

C. Mapping and Implementation

The mapping procedure required a specific set of experiments. With the objective of evaluating the amplitude of the negative sequence for each level of magnetizing current and each axial position, the rotor has been locked at different horizontal points by means of an end-stop plate and a calibrated set of spacers (Fig. 9 and Fig. 10.) The spacers have a 0.5 mm difference in length between each other. For each axial position, the level of negative sequence current has been monitored and registered using a descending sequence of magnetizing current, from the rated current down to zero. The values have been reported in a table similar to TABLE I and then transformed in the 3D LUT of Fig. 11.

Individually, the rows of TABLE I define the curve of Fig. 12. They have been implemented separately in each of the 2D *LUTs* "Axial Position Estimation" block of the scheme reported in Fig. 3. The curves define the axial position in relation to the level of the negative sequence of the carrier signal of the current.

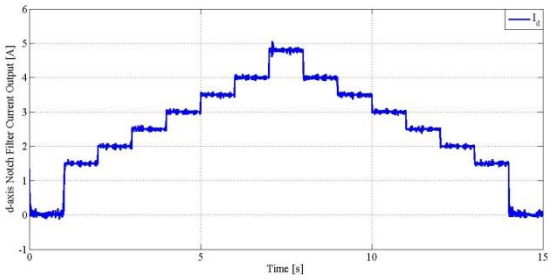

Fig. 5 - Magnetizing Current Sequence

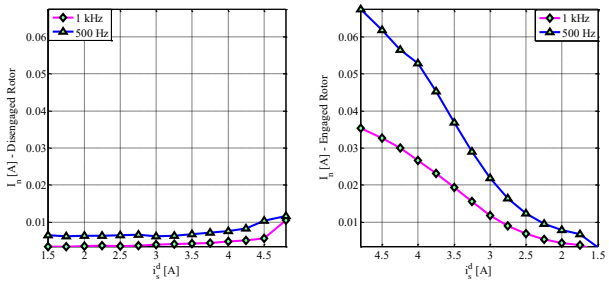

Fig. 6 - I_n trends with 500 Hz and 100Hz Injected Signal (Original Spring)

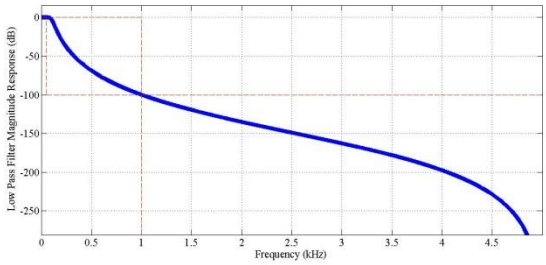

Fig. 7 - LPF Magnitude Response

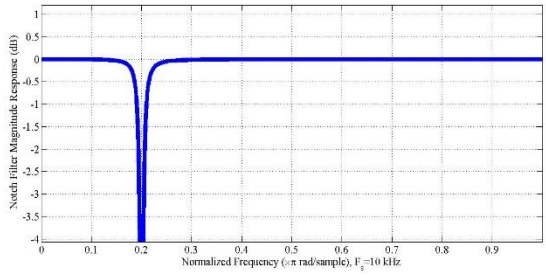

Fig. 8 - Notch Filter Magnitude Response


Fig. 9 - End Stop Plate


Fig. 10 - Set of Calibrated Spacers

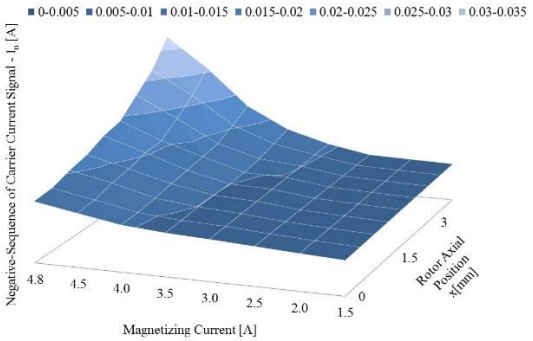

Fig. 11 - 3D LUT with 30% weaker spring

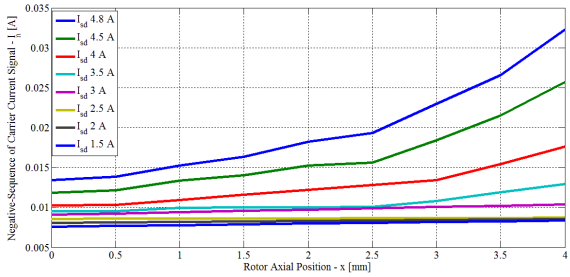

Fig. 12 - I_n vs Axial Position Curves for 2D LUT extracted from Fig. 11

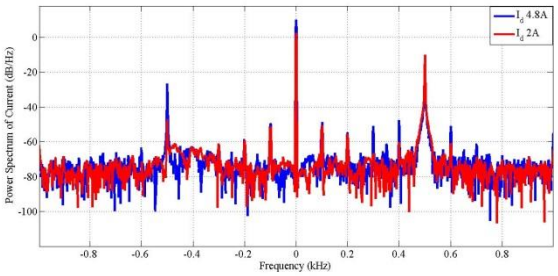

Fig. 13 - Spectrum Comparison between Disengaged and Engaged Position

IV. Axial Position Monitoring

In order to verify the axial position estimation algorithm, tests at standstill and with the rotational movement have been conducted.

A. Test At standstill

At standstill, the frequency of monitored signal will correspond to the injected frequency (500 Hz.). In Fig. 13, the spectrum of the current is reported and compared between two different cases: a) magnetizing current of 2A and disengaged rotor, b) magnetizing current of 4.8A and rotor in engaged position.

As proof that the negative counterpart of the carrier current signal is the best signal to be associated with axial position variation, amplitudes of the most evident harmonics have been recorded and compared during the engaging and disengaging phases. In correspondence of the frequency of negative-sequence, the maximum rate of variation has been recorded. Particularly, a difference of up to 20 dB in magnitude has been

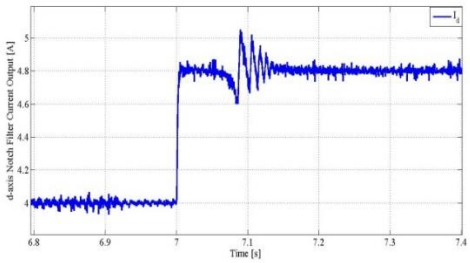

Fig. 14 - Transient in d-axis Current

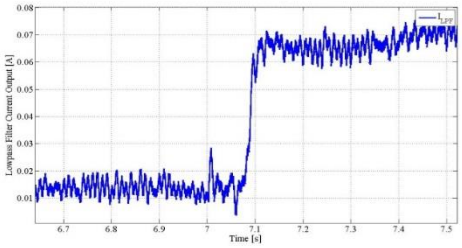

Fig. 15 - LPF Output Current (Original Spring)

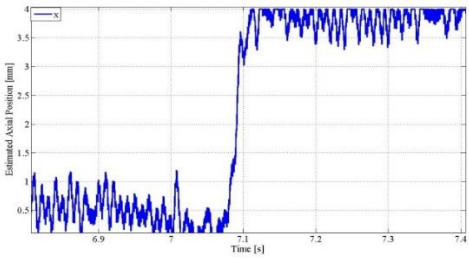

Fig. 16 - Axial Position Estimation

registered when current is lowered from 4.8A to 2A and rotor changes from engaged to disengaged position.

The I_n values, logged at standstill, were implemented in the axial position algorithm in order to check its consistency. When a sequence of magnetizing current, similar to Fig. 5, is introduced, negative-sequence current variations happen consistently. It was observed that as expected, the magnitude of the negative sequence signal, is related to the magnitude of the magnetizing current. However, when the rated current (last highest step of Fig. 5) is reached, even though the magnetizing current remains constant, an incremental step occurs in the negative-sequence signal. When the magnetizing current value is equal to 4.8A (rated value), an axial force, comparable to the spring force, is then generated and thus axial displacement or movement of the rotor is achieved. For the operating conditions mentioned above (current values and the spring), once engagement starts, a mechanical transient is observed in the magnetizing current feedback signal of Fig. 14. The machine reaches steady state in approximately 0.1s, as can be noticed in Fig. 14. During the mechanical transient, the step in the negative-sequence current amplitude occurs (Fig. 15). The output of the axial position estimation algorithm, in Fig. 16, is able to track changes in negative-sequence of the carrier current signal during this transitional phase. As can be observed in Fig. 15 and Fig. 16, the negative-sequence current

(output of the LPF) and the axial position show similar behaviors, as the axial position computational system has been optimized to be synchronized with changes in LPF current output.

B. Test with Rotational Movement and weaker spring

Tests were performed having a rotational movement and axial movement simultaneously. The rotation has been generated without using any position transducer. Due to the translational operation, the normal functioning of an encoder or resolver would have been affected. A reference speed has been generated by means of *I-f* control algorithm [40-42]. This is a scalar topology of control that enables to reach low speeds without using any position sensor.

The I-*f* method is based on separate control of $\mathbf{i_d}$, $\mathbf{i_q}$ and the generation of a reference frequency signal (f^*) to calculate a reference angle (ϑ^*).

As displayed in the I-*f* Control Block of Fig. 3, this control method consists in maintaining constant $\mathbf{i_d}$, $\mathbf{i_q}$ references and ramping the stator current frequency, as described in (15) where *k* is a positive constant [41]

$$f^* = kt^2 . \tag{15}$$

The reference angle (ϑ^*) is obtained as in (16) and utilized for the calculation of the synchronous reference frame.

$$\vartheta^* = \int 2\pi f^* dt . \tag{16}$$

Fig. 17 reports spectral analyses of the current in case of rotation. Low speed is applied (≈30rad/s). The current frequency is 5Hz. The negative sequence signal is monitored in correspondence of 490Hz.

During these tests, a different spring was used. The original spring has been replaced with a new one with 30% weaker linear coefficient spring rate (N/mm^2). The aim was to increase the time of the mechanical transient. From Fig. 18, it can be noticed that less magnetizing current is needed to overcome the spring load and reach the full engaged position. However, it is also true that with this new spring, the amplitude of the negative sequence current decreases and becomes difficult to track. Specifically, TABLE I and the 3D LUT of Fig. 11 have been built with the weaker spring. If compared with Fig. 6 and Fig. 15 (where the original spring was used), it can be noticed that the registered values of I_n, in correspondence of 4.8A and 4mm, double.

In both circumstances, when the trends of I_n, in the case of rotation, are compared with the case at standstill minor differences are found. As a consequence, the *LUT* adopted during operations at standstill will be still valid in the case of rotation. Fig. 18 and Fig. 19 show the measured values of I_n in the case of rotational movement and standstill, respectively with original and weaker spring, where in both cases, the performances of the axial position algorithm are similar to those reported in Fig. 16.

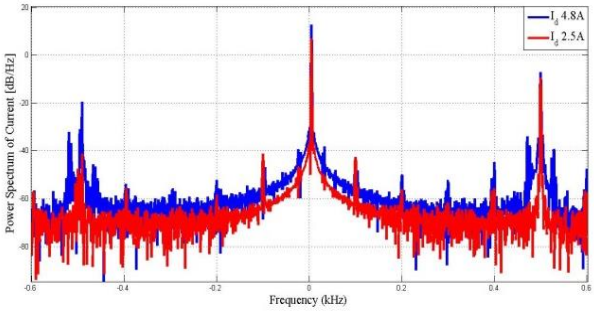

Fig. 17 - Spectrum Comparison with I-f Ctrl

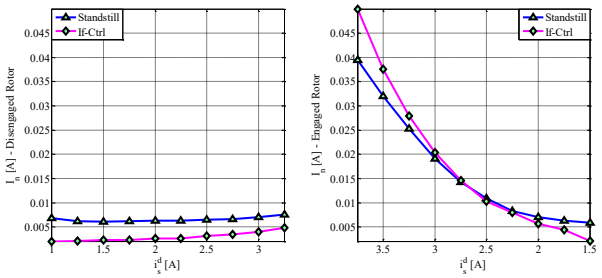

Fig. 18 - I_n Comparison at Standstill and Rotation (30% Weaker Spring)

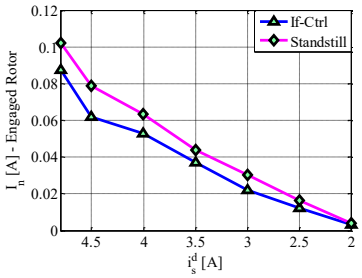

Fig. 19 - I_n Comparison at Standstill and Rotation (Original Spring)

V. CONCLUSIONS

The paper shows an innovative application of a conical shaped motor for an aerospace traction application. The motor could represent a solution for avoiding active clutch mechanisms in applications where engagement/disengagement is required. Through the realization of an axial position observer, it is possible to evaluate the axial position of the actuator without having to rely on transducers. A self-commissioning scheme for the axial position estimation has been set up through the use of high-frequency injection technique. Due to the novelty of the problem, no terms of comparison were found in the actual state-of-the-art. However, the most convenient way to estimate the axial position was found to be the tracking of saliency by means of the negative sequence of the carrier current signal. As shown, this sequence appears to be very sensitive to changes of main flux passing from disengaged to engaged position. A sensor-less axial position estimation will allow evaluating the rotor movement without any extra sensor, in order to safely and actively engage and disengage the WA from the LG.

TABLE I
MEASURED NEGATIVE-SEQUENCE OF CARRIER CURRENT SIGNAL AT DIFFERENT LEVEL OF MAGNETIZING CURRENT AND AXIAL ROTOR POSITION WITH 30% WEAKER SPRING

i_s^d	Rotor Axial Position - x								
	0 mm	**0.5 mm**	**1 mm**	**1.5 mm**	**2 mm**	**2.5 mm**	**3 mm**	**3.5 mm**	**4 mm**
4.8 A	0.0134	0.0138	0.0153	0.0163	0.0183	0.0193	0.0230	0.0266	0.0323
4.5 A	0.0118	0.0121	0.0134	0.0141	0.0153	0.0156	0.0184	0.0215	0.0257
4.0 A	0.0103	0.0103	0.0110	0.0116	0.0122	0.0128	0.0135	0.0154	0.0176
3.5 A	0.0095	0.0096	0.0100	0.0100	0.0100	0.0101	0.0108	0.0119	0.0130
3.0 A	0.0091	0.0093	0.0094	0.0096	0.0097	0.0099	0.0101	0.0102	0.0104
2.5 A	0.0086	0.0086	0.0086	0.0086	0.0086	0.0087	0.0087	0.0087	0.0087
2.0 A	0.0081	0.0081	0.0082	0.0082	0.0083	0.0084	0.0084	0.0085	0.0085
1.5 A	0.0076	0.0077	0.0078	0.0079	0.0080	0.0081	0.0082	0.0083	0.0084

ACKNOWLEDGMENT

This work was partly supported by the "EU FP7 funding via the Clean Sky JTI – Systems for Green Operations ITD".

This work was also partly funded by the European Commission under the project titled INNOVATE, FP7 project number 608322 which is part of the FP7-PEOPLE-2013-ITN call and is hosted by the Institute for Aerospace Technology at the University of Nottingham.

REFERENCES

[1] T. F. Johnson. Electric Green Taxiing System (EGTS) for Aircraft [Online]. Available: http://tec.ieee.org/newsletter/march-april-2014/electric-green-taxiing-system-egts-for-aircraft

[2] M. S. Hellstern, R. Frank, and Heribert, "Electric Wheel Hub Motor for Aircraft Application," *1*, 2012-01-14 2012.

[3] T. F. Johnson, "Electric Green Taxiing System (EGTS) for Aircraft," in *IEEE Transactions on Transportation Electrification Web Portal*, ed, 2016.

[4] M. Schier, F. Rinderknecht, A. Brinner, and H. Hellstern, "High integrated Electric Machine for Aircraft Autonomous Taxiing," in *International Conference on Electric Vehicles and Renewable Energies EVER*, 2011, p. 31.

[5] WheelTug. (2016). *WheelTug*. Available: http://www.wheeltug.com/index.php

[6] N. Gilleran, R. M. Sweet, J. S. Edelson, R. T. Cox, and I. W. Cox, "Electric Motor Integrated with a Wheel," ed: Google Patents, 2012.

[7] R. W. Jenny, "Aircraft wheel drive apparatus and method," ed: Google Patents, 1976.

[8] S. Sullivan, "Landing gear method and apparatus for braking and maneuvering," ed: Google Patents, 2007.

[9] J. Edelson and I. Cox, "Geared wheel motor design," ed: Google Patents, 2007.

[10] R. M. Sweet and J. S. Edelson, "Motor and gearing system for aircraft wheel," ed: Google Patents, 2013.

[11] I. W. Cox, H. J. Walitzki, and J. S. Edelson, "Motor for driving aircraft, located adjacent to undercarriage wheel," ed: Google Patents, 2012.

[12] Z. Xu, M. Galea, C. Tighe, T. Hamiti, C. Gerada, and S. J. Pickering, "Mechanical and thermal management design of a motor for an aircraft wheel actuator," in *2014 17th International Conference on Electrical Machines and Systems (ICEMS)*, 2014, pp. 3268-3273.

[13] M. Galea, C. Gerada, T. Raminosoa, and P. Wheeler, "A Thermal Improvement Technique for the Phase Windings of Electrical Machines," *IEEE Transactions on Industry Applications*, vol. 48, pp. 79-87, 2012.

[14] M. Galea, S. Roggia, L. Papini, Z. Xu, C. Tighe, M. Hamiti, *et al.*, "Design aspects of a high torque density machine for an aerospace traction application," in *Electrical Machines and Systems (ICEMS), 2014 17th International Conference on*, 2014, pp. 2773-2778.

[15] T. Raminosoa, T. Hamiti, M. Galea, and C. Gerada, "Feasibility and electromagnetic design of direct drive wheel actuator for green taxiing," in *2011 IEEE Energy Conversion Congress and Exposition*, 2011, pp. 2798-2804.

[16] T. Costlow. (2013). *Green taxiing machines* Available: http://articles.sae.org/12662/

[17] S. Roggia, M. Galea, C. Gerada, and F. Cupertino, "Axial position estimation of conical shaped motor for green taxiing application," in *2016 IEEE Energy Conversion Congress and Exposition (ECCE)*, 2016, pp. 1-6.

[18] H. Bitsch and H. Mall, "Sliding rotor motor," ed: Google Patents, 1992.

[19] G. Munteanu, A. Binder, and S. Dewenter, "Five-axis magnetic suspension with two conical air gap

bearingless PM synchronous half-motors," in *Power Electronics, Electrical Drives, Automation and Motion (SPEEDAM), 2012 International Symposium on*, 2012, pp. 1246-1251.

[20] Demag. (2016). *Demag Conical-rotor brake motors*. Available: http://www.demagcranes.co.uk/Drives/Motors/Conical-rotor-brake-motors

[21] J. Holtz, "Sensorless Control of Induction Machines—With or Without Signal Injection?," *IEEE Transactions on Industrial Electronics*, vol. 53, pp. 7-30, 2005.

[22] M. Pacas, "Sensorless Drives in Industrial Applications," *IEEE Industrial Electronics Magazine*, vol. 5, pp. 16-23, 2011.

[23] F. Gabriel, F. D. Belie, X. Neyt, and P. Lataire, "High-Frequency Issues Using Rotating Voltage Injections Intended For Position Self-Sensing," *IEEE Transactions on Industrial Electronics*, vol. 60, pp. 5447-5457, 2013.

[24] J. Holtz, "Sensorless control of induction motor drives," *Proceedings of the IEEE*, vol. 90, pp. 1359-1394, 2002.

[25] J. W. Finch and D. Giaouris, "Controlled AC electrical drives," *IEEE Transactions on Industrial Electronics*, vol. 55, pp. 481-491, 2008.

[26] P. P. Acarnley and J. F. Watson, "Review of position-sensorless operation of brushless permanent-magnet machines," *IEEE Transactions on Industrial Electronics*, vol. 53, pp. 352-362, 2006.

[27] J. I. Ha, "Analysis of Inherent Magnetic Position Sensors in Symmetric AC Machines for Zero or Low Speed Sensorless Drives," *IEEE Transactions on Magnetics*, vol. 44, pp. 4689-4696, 2008.

[28] F. Briz, M. W. Degner, A. Diez, and R. D. Lorenz, "Measuring, modeling, and decoupling of saturation-induced saliencies in carrier-signal injection-based sensorless AC drives," *IEEE Transactions on Industry Applications*, vol. 37, pp. 1356-1364, 2001.

[29] F. Briz, M. W. Degner, P. Garcia, and R. D. Lorenz, "Comparison of saliency-based sensorless control techniques for AC machines," *IEEE Transactions on Industry Applications*, vol. 40, pp. 1107-1115, 2004.

[30] P. L. Jansen and R. D. Lorenz, "Transducerless field orientation concepts employing saturation-induced saliencies in induction machines," *IEEE Transactions on Industry Applications*, vol. 32, pp. 1380-1393, 1996.

[31] S. Damkhi, M. S. N. Said, and N. N. Said, "Slotting effects and high frequency signal injection for induction machine rotor speed estimation," in *Electrical and Power Engineering (EPE), 2012 International Conference and Exposition on*, 2012, pp. 401-408.

[32] M. W. Degner and R. D. Lorenz, "Using multiple saliencies for the estimation of flux, position, and velocity in AC machines," *IEEE Transactions on Industry Applications*, vol. 34, pp. 1097-1104, 1998.

[33] H. Zatocil, "Sensorless control of AC machines using high-frequency excitation," in *Power Electronics and Motion Control Conference, 2008. EPE-PEMC 2008. 13th*, 2008, pp. 1024-1032.

[34] P. L. Jansen and R. D. Lorenz, "Transducerless position and velocity estimation in induction and salient AC machines," in *Proceedings of 1994 IEEE Industry Applications Society Annual Meeting*, 1994, pp. 488-495 vol.1.

[35] M. W. Degner and R. D. Lorenz, "Position estimation in induction machines utilizing rotor bar slot harmonics and carrier-frequency signal injection," *IEEE Transactions on Industry Applications*, vol. 36, pp. 736-742, 2000.

[36] N. Teske, G. M. Asher, M. Sumner, and K. J. Bradley, "Analysis and suppression of high-frequency inverter modulation in sensorless position-controlled induction machine drives," *IEEE Transactions on Industry Applications*, vol. 39, pp. 10-18, 2003.

[37] N. Teske, G. M. Asher, M. Sumner, and K. J. Bradley, "Suppression of saturation saliency effects for the sensorless position control of induction motor drives under loaded conditions," *IEEE Transactions on Industrial Electronics*, vol. 47, pp. 1142-1150, 2000.

[38] H. Zatocil, "Physical understanding of multiple saliencies in induction motors and their impact on sensorless control," in *Power Electronics, Electrical Drives, Automation and Motion, 2008. SPEEDAM 2008. International Symposium on*, 2008, pp. 1503-1508.

[39] V. K. Ingle and J. G. Proakis, *Digital Signal Processing Using MATLAB*: Cengage Learning, 2011.

[40] I. Boldea, A. Moldovan, and L. Tutelea, "Scalar V/f and I-f control of AC motor drives: An overview," in *2015 Intl Aegean Conference on Electrical Machines & Power Electronics (ACEMP), 2015 Intl Conference on Optimization of Electrical & Electronic Equipment (OPTIM) & 2015 Intl Symposium on Advanced Electromechanical Motion Systems (ELECTROMOTION)*, 2015, pp. 8-17.

[41] L. I. Iepure, I. Boldea, and F. Blaabjerg, "Hybrid I-f Starting and Observer-Based Sensorless Control of Single-Phase BLDC-PM Motor Drives," *IEEE Transactions on Industrial Electronics*, vol. 59, pp. 3436-3444, 2012.

[42] S. C. Agarliță, M. Fătu, L. N. Tutelea, F. Blaabjerg, and I. Boldea, "I-f starting and active flux based sensorless vector control of reluctance synchronous motors, with experiments," in *2010 12th International Conference on Optimization of Electrical and Electronic Equipment*, 2010, pp. 337-342.